



Experimental characterization and finite element simulation of FDM 3D printed polymer composite tooling for sheet metal stamping

Madhura Athale¹ · Taejoon Park² · Ryan Hahnen³ · Farhang Pourboghra^{1,2}

Received: 20 April 2022 / Accepted: 14 July 2022 / Published online: 26 July 2022
© The Author(s), under exclusive licence to Springer-Verlag London Ltd., part of Springer Nature 2022

Abstract

3D printed polymer composite materials offer a cost-effective and rapid tooling option for prototyping, and low-cost, low-volume sheet metal forming applications. Due to the high anisotropy in mechanical properties of 3D printed composites, accurate characterization and finite element modeling of the material become paramount for successful design and application of these forming tools. This paper presents experimental characterization of 3D printed fiber-reinforced polymer composite material at various strain rates. A homogenized material model with orthotropic elasticity and the Hill 1948 anisotropic yield criterion were then calibrated based on these experimental data. Finite element simulations of the stamping of high-strength steel sheets using composite tooling were performed, and tool deformation was predicted and compared with experimental measurements. FE simulation results were in good agreement with stamping experiments performed with polymer tooling. It was found that the anisotropy and strain rate sensitivity of 3D printed polymer composites play a significant role in their performance as tooling materials.

Keywords 3D printing · Anisotropy · Mechanical testing · Finite element analysis (FEA)

1 Introduction

Additive manufacturing (AM) has gained popularity due to its cost-effectiveness, quick fabrication, as well as flexibility and ease of fabricating various intricate structures which can be challenging to fabricate by conventional methods [1]. Early AM applications were limited to models, prototypes, and low-load parts [2]. With the technological advancement of AM over the last couple of decades, the quality of AM parts in terms of dimensional accuracy and strength is improving significantly [3]. This has led to the use of AM in real-time industrial applications in automotive, aerospace, electronics, construction, military, and biomedical sectors [4–6].

The automotive sector is facing challenges to develop manufacturing processes suitable to accommodate for shorter product lifecycles, increasing variety due to high levels of customization in case of luxury vehicles, saving time and cost for small and medium-scale production etc. [4, 5]. Automotive manufacturing has large volumes of parts with over 1000 vehicles per line per day, where sheet metal forming becomes attractive due to its cost-effectiveness for large volume production. Conventional stamping tools have high initial cost due to skilled labor required and long lead time, making it expensive to produce small scale or prototype parts. Use of AM technology to produce support structures such as dies and tools offers an economic advantage for small and medium volume production, while also allowing for design flexibility which is unavailable in conventional stamping tools [9–11]. Material and method selection should be done to satisfy the functional requirements of metal forming tools namely – dimensional accuracy, wear resistance, cost, surface performance, fracture and fatigue strength, and reparability [12].

Among various AM technologies, fused deposition modeling (FDM) or fused filament fabrication (FFF) is one of the most common methods for producing polymer AM parts. Polymer AM is cheaper than metal AM due to

✉ Farhang Pourboghra
pourboghra.2@osu.edu

¹ Department of Mechanical and Aerospace Engineering,
The Ohio State University, 201 W19th Ave, Columbus,
OH 43210, USA

² Department of Integrated Systems Engineering, The Ohio
State University, 210 Baker Systems 1971 Neil Avenue,
Columbus, OH 43210, USA

³ Honda Development and Manufacturing of America LLC,
Raymond, OH, USA

lower material costs as well as eliminating the need for post-production machining due to fine build resolution in most cases [9]. FDM parts are fabricated directly from CAD data, by slicing the model into several thin layers and building the part layer by layer. A polymer filament is extruded through a heated nozzle and deposited over the previous layer to build up the desired shape. Nozzle head controlled by a 3-axis system that moves in the X – Y plane according to the decided toolpath and in the Z direction after each layer is completed to build the next layer. Typically, each layer consists of material deposited along the perimeter in one or more passes and filled-in with a raster pattern. As polymer material is deposited in a semi-molten state, it fuses with the neighboring raster track and the previous layer forming a solid part. The infill density can be varied to achieve the desired properties. Several materials such as acrylonitrile butadiene styrene (ABS), polyethylene (PE), polypropylene (PP), polycarbonate (PC), polylactic acid (PLA), polyethylene terephthalate glycol (PETG), polyether ether ketone (PEEK), Nylon12, and thermoplastic elastomer (TPE) are available for use with FDM [4]. Various particles, chopped or continuous fibers such as carbon fiber, glass fiber, silica, zirconium, aluminum oxide, titanium oxide, etc. are used as fillers or reinforcements to improve the strength, stiffness, thermal and electrical properties, wear and impact resistance of the parts [3, 9]. Inclusions also improve the dimensional stability of the printed part through reduction of shrinkage and distortion [14].

FDM parts have very large anisotropy in mechanical properties due to various factors such as layer thickness, raster orientation, presence of reinforcements, and different thermal histories within the part. Extrusion forces align the reinforcement fibers along the raster direction, making the part significantly stronger in raster direction compared to the transverse direction [5]. Another important factor contributing to the high anisotropy of FDM parts is the presence of voids or porosity. As adjacent raster paths with a round cross section fuse together, molten filaments solidify before filling the entire volume, leaving voids behind. High content of reinforcements causes higher viscosity of the melt leading to higher number of pores due to the inability of the melt bead to spread to fill the gaps [4, 14]. Several studies have been carried out to experimentally characterize the mechanical properties of AM materials [4, 5, 15–19], as well as analytical and numerical modeling to predict mechanical properties [15, 20–26].

Use of polymer [4] tools for sheet metal forming is being actively investigated by many researchers using experimental as well as modeling and simulation approaches [11, 12, 27, 28]. Frohn-Soerensen et al. demonstrated the use of additively manufactured PLA tools for rubber pad stretch forming of DC03 sheets in a 64-part trial and noted some

deviations in the tool as well as the stamped part dimensions [10]. The authors in [3] and [29] have investigated the use of PLA AM tools for V-bending of aluminum and steel sheets. AM tools made of PLA, PET, and thermosetting polymer composite Ren Shape 5166 have also been used successfully for deep drawing of 1000 series aluminum, various mild Steels, and SS304 sheets [3, 8, 30, 31]. Durgun formed 100 parts from DC04 and MC355 sheets using FDM polycarbonate dies and found that while DC04 parts were within the tolerance range, MC355 parts had large deviations beyond the dimensional tolerance. MC355 material is harder than DC04 which caused significant geometric deviation in the FDM dies due to squeezing of FDM layers resulting in poor dimensional tolerance beyond 50 parts [32]. Kuo and Li studied the performance of sheet metal forming tools made with epoxy resin and various filler materials such as Al and zirconia particles for forming Al–Mg alloy sheets in a 20-part trial and found that the addition of Al and ZrO_2 particles improved the wear resistance of epoxy dies [13].

Finite element (FE) simulation is a powerful tool for the design optimization and performance prediction of sheet metal forming dies [33]. Park and Colton performed FE and experimental studies on fatigue limit testing of polymer V-bending dies and the effect of process parameters on the same. They concluded that the maximum principal stress is a better failure criterion than the effective stress due to the polymer's low ductility [34]. Liewald and de Souza investigated the tribological properties of polyurethane with aluminum hydroxide fillers with various steel sheets to characterize the friction and wear behavior of the tools. They performed FE simulations of the stamping of steel sheets using polyurethane and epoxy dies using an isotropic material model for the polymer dies [7]. Schuh et al. performed cup drawing FE simulations of DC01 sheet with an isotropic material model for AM PLA dies [8].

Few studies have been carried out using FE simulations for prediction of polymer tool life based on fatigue, fracture, wear, and plastic deformation. The evolution of tool damage and deformation with successive stamping passes needs to be studied as a step towards tool life prediction. The effect of anisotropic mechanical properties on the tool performance is a critical aspect which needs attention for successful die design. Additionally, the ability of FDM polymer tools to stamp stronger materials such as high-strength steels needs to be investigated to realize their full potential in the stamping industry. To bridge these gaps, in this paper, the authors focused on evaluating the feasibility of using FDM polymer composite as low-cost tooling for stamping of high-strength steel (HSS) sheets through experimental and FE simulation methods. Below are the steps taken as part of this investigation.

- Experimentally characterized the anisotropic mechanical properties of carbon fiber filled Nylon 12 (Nylon 12CF) tooling material fabricated with FDM.
- Developed and calibrated a homogenized material model based on orthotropic elasticity and the Hill 1948 anisotropic yield criterion to represent the mechanical behavior of the FDM tool.
- Performed multiple FE simulations of the stamping of DP 590 high-strength steel sheets with progressively deforming FDM tool. To that end, the geometry of the FDM tool was updated after each FE simulation. To verify simulation results, the amount of damage to the FDM tool was compared with experimental results.

The results from this paper clearly show that by properly modeling the mechanical behavior of the FDM tool, FE simulations can be performed to assess the performance of low-cost composite tooling for stamping of high-strength steel sheets.

2 Material testing and characterization

2.1 Materials

For this study, FDM Nylon 12CF material from Stratasys Ltd., which is polyamide 12 thermoplastic filament reinforced with 35wt% chopped carbon fiber, is used as low-cost tooling material. Nylon 12CF has high stiffness and the highest flexural strength of any FDM thermoplastic making it an ideal candidate for this application [35]. All parts are fabricated by Stratasys Ltd. using FDM with a layer thickness of 0.254 mm and raster width of 0.5 mm. A single-perimeter raster is used in each layer, filled-in with a crisscross raster and 100% infill density. Since the fibers are stiffer and stronger than the matrix by orders of magnitude along their longitudinal direction, the macroscopic properties of the part are highly anisotropic. Alternating orthogonal arrangement of raster through the part thickness results in the final part having a tetragonal symmetry with 5 mirror planes as shown in Fig. 1, where X – Y is the build plane with raster orientation of $\pm 45^\circ$ from the X axis and Z is the build direction. Thus, the two in-plane directions X and Y are equivalent or identical and so are the two diagonal directions XZ and YZ . Out of 3 principal and 3 diagonal directions, there are only 4 unique directions due to the symmetry.

DP 590, which is a high-strength steel, is used as the blank material with initial thickness of 1.539 mm. The following subsections detail the experimental procedure used to conduct uniaxial tension and uniaxial compression tests on the FDM composite material, as well as uniaxial tension tests on the blank material.

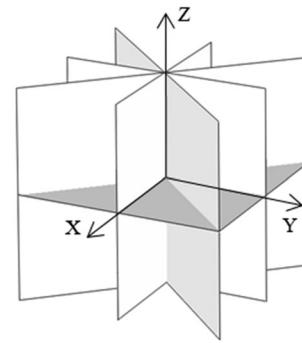


Fig. 1 Symmetry planes for tetragonal symmetry

2.2 FDM composite material testing

2.2.1 Uniaxial tension

To fully characterize the FDM material, uniaxial tensile tests in 4 unique directions as shown in Fig. 2 were performed. Tensile samples as shown in Fig. 2 having a square cross section were machined from a 3D printed block of Nylon 12CF. A sample geometry having a square cross section was considered to include as many raster layers as possible in consideration of the thickness of each raster while using the same sample geometry for each tensile direction. The ratio of length to width of the uniform elongation section was set to 2.5 to ensure uniaxial tension in the range of 5% or less strain that the tool material would experience. MTS Landmark testing machine with a 100-kN capacity load cell was used to perform the tests, and digital image correlation (DIC) system from GOM was used for strain measurement. Three samples were tested for each direction to ensure repeatability. Strain measurement was done on the front and side surface of the sample thus giving two unique Poisson's ratios and one elastic modulus from each test direction. All tensile tests were performed at a constant quasi-static strain rate of 10^{-4} /s until fracture. Figure 3 shows representative engineering stress–strain plots for each direction and Table 1 shows the averaged measured Young's moduli

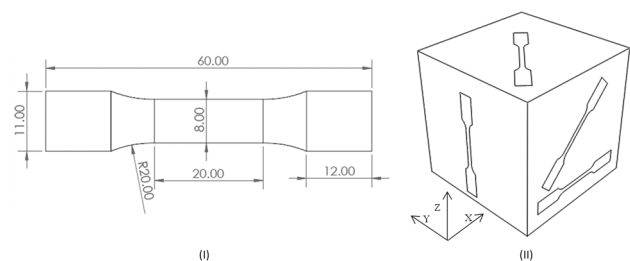


Fig. 2 I Uniaxial tension sample geometry and dimensions in mm. II Sample orientations for tensile testing

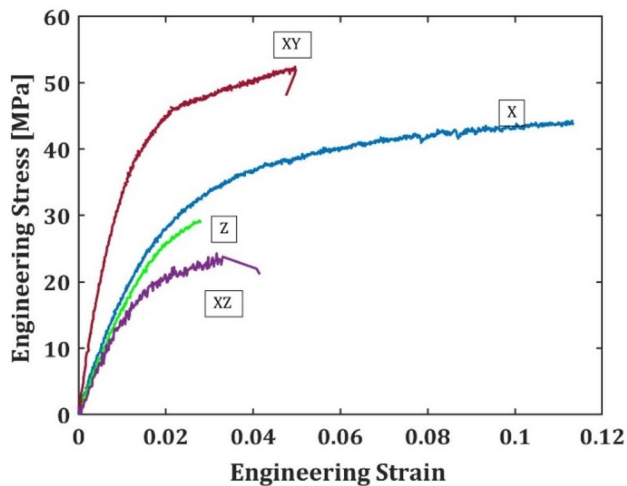


Fig. 3 Stress–strain plots for uniaxial tensile test for all tested directions

(E), Poisson's ratios (ν), and 0.2% offset yield stresses (σ_y) from the tensile tests. ν_{ij} for all principal directions is the Poisson's ratio obtained by strain measurement on the i – j plane where i is the tensile direction and j is the transverse direction. For diagonal directions, only one Poisson's ratio in the same plane as the test direction was measured ($\nu_{in-plane}$). Uniaxial tension results show significant anisotropy in both elastic and plastic behavior. As expected from the meso-structure of FDM materials with fiber reinforcements, the material is stiffest and strongest in the XY direction which has the fibers oriented at 0 – 90° with respect to the tensile direction. The XZ direction is the least stiff and weakest with tensile failure occurring due to the delamination between two layers, at 45° to the tensile direction.

2.2.2 Uniaxial compression

The presence of voids in the material as well as the evolution of the raster pattern can cause different behavior under tension vs compression. In tooling applications, the material is mostly experiencing compressive loads, making it important to characterize the materials under compression. Uniaxial compression tests were performed using the same sample geometry as that used for uniaxial tension. The short length of the samples

allowed for compression tests to be performed without the use of an anti-buckling device. Compression tests were performed on MTS Landmark machine with a 100-kN capacity load cell, and DIC was used for strain measurement. Uniaxial compression test was performed for X , Z , XY , and XZ directions at constant quasi-static strain rates. Test was carried out until the sample showed either bulging or buckling or barreling in each case. Table 2 shows the averaged experimental results from uniaxial compression tests. Figure 4 shows a comparison between representative uniaxial tension (T) and uniaxial compression (C) true stress–strain plots. Elastic behavior is nearly identical between tension and compression, while plastic behavior shows differences. In Z , XY , and XZ directions, the material shows higher stress in compression than tension beyond the point of initial yield. This could be due to voids closing under compression and providing higher strength and voids expanding under tension. In the X direction, this effect is counteracted by rotation of the fiber reinforcement inside the material. In the X direction, the fibers are oriented at $\pm 45^\circ$ to the direction of tension or compression. The fibers rotate towards the direction of applied load under tension providing additional strength to the material, whereas the fibers rotate away from the direction of load making the material weaker under compression. Fiber rotation for X direction samples is illustrated schematically in Fig. 5. Researchers have successfully modelled the behavior of fiber-reinforced composites undergoing complex deformations by accounting for the rotation of fibers inside the matrix as deformation progresses [36, 37].

2.3 DP590 material testing

2.3.1 Uniaxial tension

To characterize the blank material, uniaxial tension tests following the ASTM E8 standard were performed on samples cut from the same DP 590 blanks of 1.539-mm thickness that were used for stamping experiments. Testing was done on Instron machine with 50-kN capacity load cell, and DIC was used for strain measurement. Three samples each were tested along 0° , 45° , and 90° to the rolling direction to capture the planar anisotropy of the rolled sheets (Table 3). Figure 6 shows representative engineering stress–strain plots obtained from the 3 directions. DP 590 blanks showed small planar anisotropy in the yield

Table 1 Averaged uniaxial tension results with deviations for Nylon 12CF

| Property | Orientation | | | |
|-----------------------------------|--|--|--------------------------------|--------------------------------|
| | X | Z | XY | XZ |
| Young's modulus (E) (GPa) | 1.95 ± 0.15 | 1.72 ± 0.20 | 4.03 ± 0.35 | 1.60 ± 0.46 |
| Poisson's ratio (ν) | $\nu_{xy} = 0.64 \pm 0.05$ $\nu_{xz} = 0.20 \pm 0.01$ | $\nu_{zx} = 0.15 \pm 0.03$ $\nu_{zy} = 0.14 \pm 0.02$ | $\nu_{planar} = 0.11 \pm 0.01$ | $\nu_{planar} = 0.30 \pm 0.03$ |
| Yield stress (σ_y) (MPa) | 30.5 ± 2.6 | 26.2 ± 4.3 | 35.2 ± 0.8 | 18.9 ± 3.3 |

Table 2 Averaged uniaxial compression results with deviations for Nylon 12CF

| Property | Orientation | | | |
|-----------------------------------|--|--|--------------------------------|--------------------------------|
| | X | Z | XY | XZ |
| Young’s modulus (E) (GPa) | 2.20 ± 0.20 | 1.85 ± 0.08 | 3.95 ± 0.52 | 1.6 ± 0.55 |
| Poisson’s ratio (ν) | $\nu_{xy} = 0.55 \pm 0.05$ $\nu_{xz} = 0.25 \pm 0.04$ | $\nu_{zx} = 0.14 \pm 0.03$ $\nu_{zy} = 0.12 \pm 0.04$ | $\nu_{planar} = 0.09 \pm 0.01$ | $\nu_{planar} = 0.31 \pm 0.02$ |
| Yield stress (σ_y) (MPa) | 26.4 ± 2.51 | 29.2 ± 0.76 | 45.5 ± 1.92 | 25.8 ± 2.81 |

stress; hence, isotropic material model was used for modeling the blank in FE simulations.

3 Constitutive modeling

3.1 Orthotropic elasticity

As explained previously, 3D printed materials with orthogonal raster pattern in adjacent layers exhibit tetragonal symmetry with 5 planes of symmetry. Reducing the Hooke’s law for general anisotropic material using these symmetry operations results in the following compliance matrix for tetragonal symmetry, which is the inverse of the elastic stiffness matrix.

$$S = \begin{bmatrix} S_{11} & S_{12} & S_{13} & 0 & 0 & 0 \\ S_{12} & S_{11} & S_{13} & 0 & 0 & 0 \\ S_{13} & S_{13} & S_{33} & 0 & 0 & 0 \\ 0 & 0 & 0 & S_{44} & 0 & 0 \\ 0 & 0 & 0 & 0 & S_{44} & 0 \\ 0 & 0 & 0 & 0 & 0 & S_{66} \end{bmatrix} \quad (1)$$

The compliance matrix in (1) is written in Voigt notation using the rules given in Table 4 to convert between standard notation and Voigt notation.

The compliance matrix has 6 independent coefficients, which is a special case of orthotropic symmetry which has only 3 planes of symmetry and 9 independent coefficients. These coefficients are calibrated using experimental data from tensile tests using the following relationships.

$$S_{11} = \frac{\epsilon_{xx}}{\sigma_{xx}} = \frac{1}{E_x}; S_{33} = \frac{\epsilon_{zz}}{\sigma_{zz}} = \frac{1}{E_z} \quad (2)$$

$$S_{12} = \frac{-\nu_{xy}}{E_x} = \frac{-\nu_{yx}}{E_y}; S_{13} = \frac{-\nu_{xz}}{E_x} = \frac{-\nu_{yz}}{E_y} = \frac{-\nu_{zx}}{E_z} \quad (3)$$

where ϵ_{ii} , σ_{ii} , and E_i are the measured longitudinal strain, measured true stress, and elastic modulus, respectively, when i is the direction of uniaxial tension. ν_{ij} is the Poisson’s ratio defined as $-\epsilon_{ij}/\epsilon_{ii}$ where i is the tensile direction and j is the transverse direction. The shear components are calibrated from tensile tests performed along diagonal direction between two principal directions.

Fig. 4 Comparison of uniaxial tension (T) and uniaxial compression (C) stress–strain plots for all tested directions

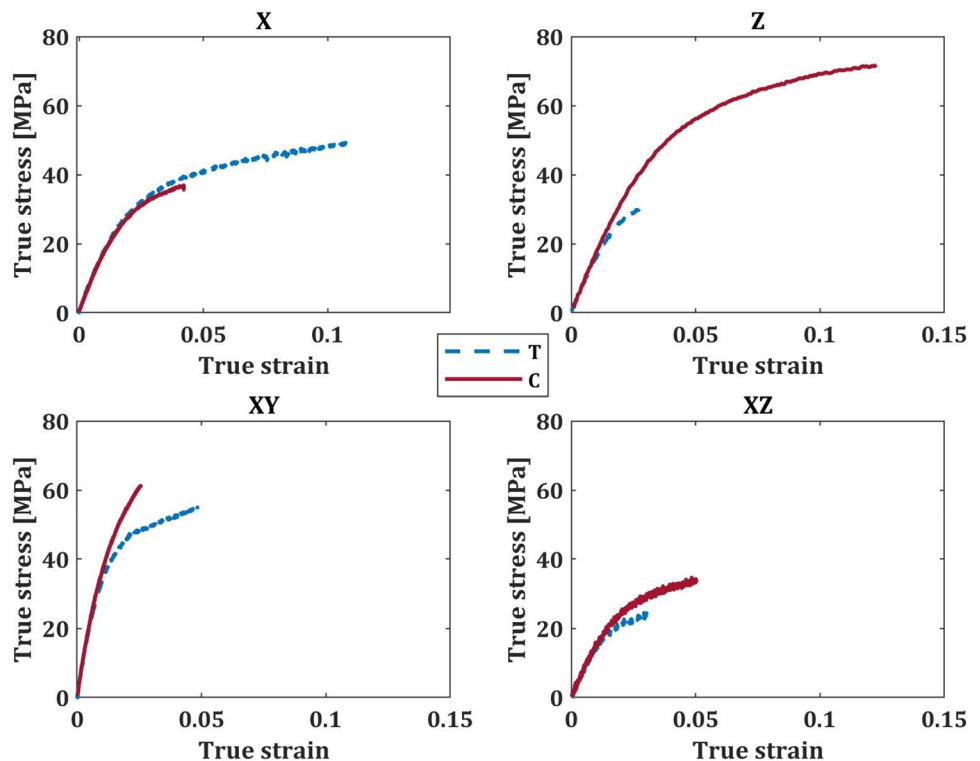
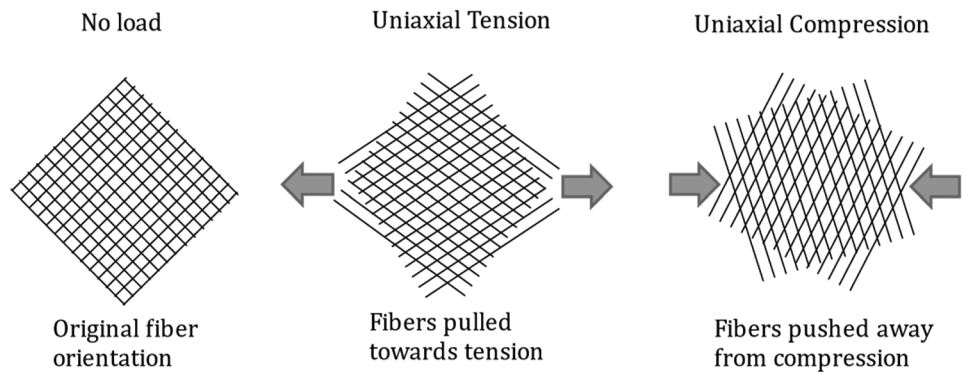


Fig. 5 Fiber rotation under applied tension and compression for X direction samples



$$S_{66} = \frac{2(\epsilon_{xy45_longitudinal} - \epsilon_{xy45_transverse})}{\sigma_{xy45}} \tag{4}$$

$$S_{44} = \frac{2(\epsilon_{xy45_longitudinal} - \epsilon_{xy45_transverse})}{\sigma_{xy45}} \tag{5}$$

where σ_{ij45} is the measured true stress and $\epsilon_{ij45_longitudinal}$ and $\epsilon_{ij45_transverse}$ are the measured strains in the longitudinal and transverse directions, respectively, when uniaxial tension test is performed in the diagonal direction in $i-j$ plane at 45° to both axes.

The stiffness matrix is then obtained by taking the inverse of compliance matrix as shown below and satisfies the Hooke’s law ($[\sigma] = [C][\epsilon^e]$):

$$S = \begin{bmatrix} \frac{1-v_{xz}v_{zx}}{E_x E_z \Delta} & \frac{v_{xy}+v_{xz}v_{zx}}{E_x E_z \Delta} & \frac{v_{zx}+v_{xy}v_{zx}}{E_x E_z \Delta} & 0 & 0 & 0 \\ \frac{v_{xy}+v_{xz}v_{zx}}{E_x E_z \Delta} & \frac{1-v_{xz}v_{zx}}{E_x E_z \Delta} & \frac{v_{zx}+v_{xy}v_{zx}}{E_x E_z \Delta} & 0 & 0 & 0 \\ \frac{v_{zx}+v_{xy}v_{zx}}{E_x E_z \Delta} & \frac{v_{zx}+v_{xy}v_{zx}}{E_x E_z \Delta} & \frac{1-v_{xy}v_{zx}}{E_x^2 \Delta} & 0 & 0 & 0 \\ 0 & 0 & 0 & 2G_{xz} & 0 & 0 \\ 0 & 0 & 0 & 0 & 2G_{zx} & 0 \\ 0 & 0 & 0 & 0 & 0 & 2G_{xy} \end{bmatrix} \tag{6}$$

where,

$$\Delta = \frac{1 - v_{xy}^2 - 2v_{xz}v_{zx} - 2v_{xy}v_{zx}v_{xz}}{E_x^2 E_z}$$

In the uniaxial tension and compression test results shown in the previous section, the elastic behavior of the 3D printed composites is identical in tension and compression, thus either

Table 3 Averaged experimental results from uniaxial tension test of DP590 for 3 different angles from rolling direction (RD)

| Property | Angle from RD | | |
|-----------------------------------|---------------|-------|-------|
| | 0° | 45° | 90° |
| Young’s modulus (E) (GPa) | 206.5 | 211.6 | 220.2 |
| Poisson’s ratio (ν) | 0.31 | 0.29 | 0.30 |
| Yield stress (σ_y) (MPa) | 435.2 | 456.6 | 470.1 |

of the two can be used to calibrate the orthotropic stiffness matrix. Table 5 shows the 6 independent elastic coefficients of the elastic stiffness matrix determined for CF-Nylon.

3.2 Plastic anisotropy

To model the plastic behavior of the composite tooling, Hill’s 1948 yield criterion is used along with isotropic hardening rule. The general 3D version of Hill’s 1948 yield function is

$$F(\sigma_{yy} - \sigma_{zz})^2 + G(\sigma_{zz} - \sigma_{xx})^2 + H(\sigma_{xx} - \sigma_{yy})^2 + 2L\sigma_{yz}^2 + 2M\sigma_{zx}^2 + 2N\sigma_{xy}^2 = \sigma^{-2} \tag{7}$$

Here, $\bar{\sigma}$ is the effective stress and $F, G, H, L, M,$ and N are anisotropy coefficients. Due to tetragonal symmetry, X and Y directions are equivalent as are XZ and YZ directions. This gives us the following two relations.

$$\begin{aligned} L &= M \\ G + H &= F + H \end{aligned} \tag{8}$$

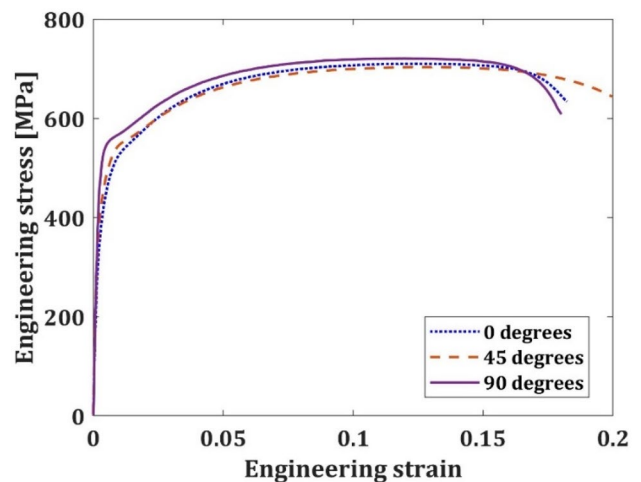


Fig. 6 Engineering stress vs. strain plot obtained from uniaxial tension tests on DP590 in 3 directions

Table 4 Conversion from standard notation to Voigt notation

| Standard notation | Voigt notation | Standard notation | Voigt notation |
|-------------------|----------------|-------------------|----------------|
| <i>xx</i> | 1 | <i>yz</i> | 4 |
| <i>yy</i> | 2 | <i>xz</i> | 5 |
| <i>zz</i> | 3 | <i>xy</i> | 6 |

Using the measured true stress in *X*, *Z*, *XY*, and *XZ* directions in (7), we get four additional relations. The 6 anisotropy coefficients can be obtained using the following equations [38].

$$\begin{aligned}
 F = G &= \frac{1}{2} \left(\frac{\bar{\sigma}}{S_Z} \right)^2; & H &= \left(\frac{\bar{\sigma}}{S_Z} \right)^2 - \frac{1}{2} \left(\frac{\bar{\sigma}}{S_Z} \right)^2 \\
 N &= 2 \left[\left(\frac{\bar{\sigma}}{S_{XY}} \right)^2 - \frac{1}{4} \left(\frac{\bar{\sigma}}{S_Z} \right)^2 \right]; & & (9) \\
 L = M &= 2 \left[\left(\frac{\bar{\sigma}}{S_{XZ}} \right)^2 - \frac{1}{4} \left(\frac{\bar{\sigma}}{S_X} \right)^2 \right]
 \end{aligned}$$

where *S_X*, *S_Z*, *S_{XY}*, *S_{XZ}* are corresponding measured flow stresses from uniaxial tensile tests performed in *X*, *Z*, *XY*, and *XZ* directions for equivalent plastic work, respectively. Since plastic behavior in compression is more important for tooling applications, stresses from uniaxial compression test are used to calibrate the Hill 1948 yield function for CF-Nylon. Calibrated coefficients with $\bar{\sigma}$ for Hill 1948 yield function are given in Table 6.

Hill’s 48 yield function was used for the simplicity of calibrating as well as accessibility, because the yield function is already available in Abaqus explicit solver. More advanced yield criteria such as the modified Drucker-Prager yield criterion can be used to model tension–compression asymmetry [39, 40]. As for the isotropic hardening rule, effective stress-equivalent plastic strain curve was obtained from the compression test in *Z* direction up to 5% true strain range. For FE simulations, the hardening law was used in the form of tabular reference hardening data for FE simulations.

3.3 Material characterization validation

AM material model calibration is validated by performing single-element uniaxial compression FE simulations

Table 5 Calibrated coefficients for tetragonal stiffness matrix (GPa)

| <i>C</i> ₁₁ | <i>C</i> ₁₂ | <i>C</i> ₁₃ | <i>C</i> ₃₃ | <i>C</i> ₄₄ | <i>C</i> ₆₆ |
|------------------------|------------------------|------------------------|------------------------|------------------------|------------------------|
| 3.879 | 2.721 | 1.179 | 2.122 | 0.621 | 1.802 |

Table 6 Calibrated coefficients for Hill 1948 yield function

| <i>F</i> | <i>G</i> | <i>H</i> | <i>L</i> | <i>M</i> | <i>N</i> |
|----------|----------|----------|----------|----------|----------|
| 0.5 | 0.5 | 1.858 | 4.291 | 4.291 | 0.979 |

in ABAQUS/Explicit along the 4 unique material directions and comparing the results with experimental data. A single 8-noded linear brick element with one integration point (C3D8R) and enhanced hourglass control was used along with the boundary conditions as shown in Fig. 7. Displacement boundary conditions on opposite faces of the cubic element were used to achieve uniaxial compression loading similar to the experiments. Single integration point in the element gives uniform distribution of displacement throughout the element. AM material was modeled by the orthotropic linear elasticity model assuming tetragonal symmetry and Hill 1948 anisotropic yield function with a reference hardening curve obtained from uniaxial compression test along the *Z* direction. Calibrated coefficients from Tables 5 and 6 were used to define the material behavior in the simulations. Figure 8 shows that FE simulations are in good agreement with the experiments in both elastic and plastic deformation for all tested directions, thus validating the material model calibration.

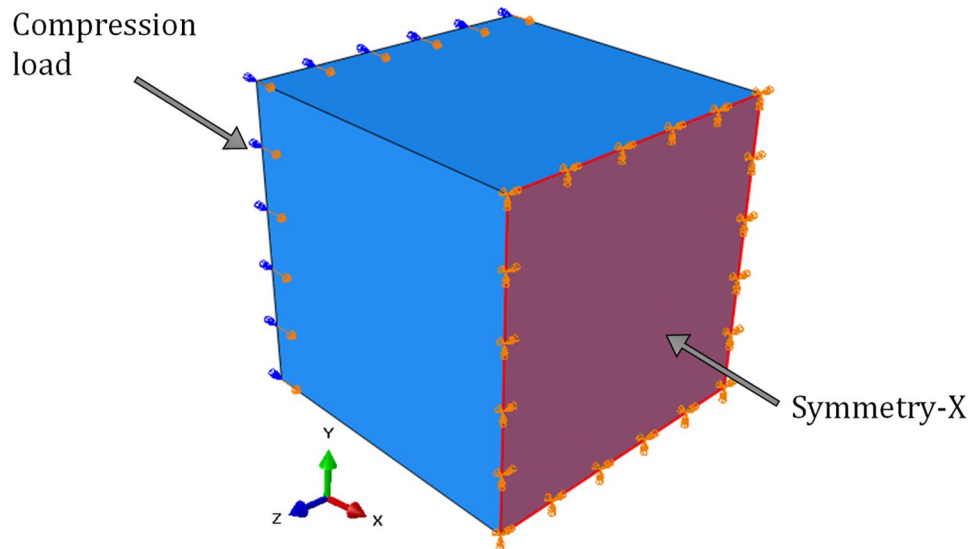
4 Stamping with lab-scale 3D printed tools

4.1 Experiments

To assess the performance of composite 3D-printed materials as stamping tools, the lab-scale die geometry shown in Fig. 9 was selected. The selected geometry has convex, concave, and flat sections along the die radius, causing the sheet and tools to experience complex multiaxial stresses. This makes the geometry ideal for evaluating the tool performance, and the results can potentially be extrapolated to full-scale automotive stamping tools.

Existing conventional dies made of tool steel were used to stamp 100 parts from 1.539-mm thickness DP 590 blanks as a “Baseline” to be used for comparison with polymer dies. As an initial trial, only the die insert was fabricated with CF-Nylon using FDM. The printed insert was then attached to the remaining preexisting die made of steel. The punch in this case was also made of steel. This tool set was also used to stamp 100 sheets of 1.539-mm-thick DP 590 steel. Steel tools as well as the modified die with FDM insert are shown in Fig. 10. A punch stroke of 65 mm and blank holding force of 200

Fig. 7 FE simulation geometry and boundary conditions for material model verification showing compression along X direction



kN were used for all experiments. Figure 11 shows the punch speed and stroke profile. All blank sheets were coated with Cool Form[®] lubricant prior to stamping to lower friction.

The 3D-printed tools were scanned using ATOS 3D scanner developed by GOM before and after the 100-part stamping trials to quantify the geometry change due to plastic deformation, damage, and wear. Every 10th stamped part was analyzed using ARGUS strain measurement system to quantify any deviations in parts resulting from tool geometry changes. Parts #1, #50, and #100 were scanned using ATOS 3D scanner, and the scans were compared with that of parts made with conventional steel tooling to assess whether composite tooling can successfully

replace conventional tooling for low-volume production while maintaining good geometric tolerance of the stamped parts.

4.2 FE simulations

Finite element simulations of the stamping process were performed on the commercial software ABAQUS/Explicit. For stamping with steel tools, all the tools were modeled as rigid parts. For CF-Nylon simulations, the die insert was modeled using 2-mm deformable linear tetrahedral elements (C3D4) while the rest of the die and punch were modeled as rigid as shown in Fig. 12. The blank holder was modeled as rigid since a steel holder was used in all experiments. The blank was meshed with 3-mm shell elements having 7 Gauss integration points through thickness. Element type and size for each part were decided based on a mesh sensitivity analysis considering parameters such as the stresses and strains at critical locations. Die was fixed while the punch was given a displacement boundary condition with the same profile as in experiments. Friction coefficient between the blank and tools was calibrated for steel tools as well as polymer tools by comparing the punch force vs. displacement data from experiments and simulations as shown in Fig. 13. A friction coefficient of 0.15 was found to be ideal for both steel and polymer tools.

To quantify the effect of orthotropic elasticity vs isotropic elasticity as well as the use of anisotropic yield function such as Hill 1948 on the simulation results, 3 different simulations were performed. Material models for the polymer tools in the 3 simulations were as follows:

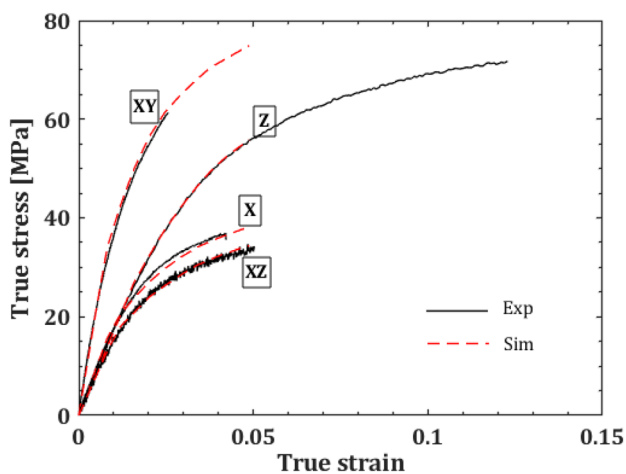


Fig. 8 Comparison of experimental and simulation stress–strain curves for uniaxial compression

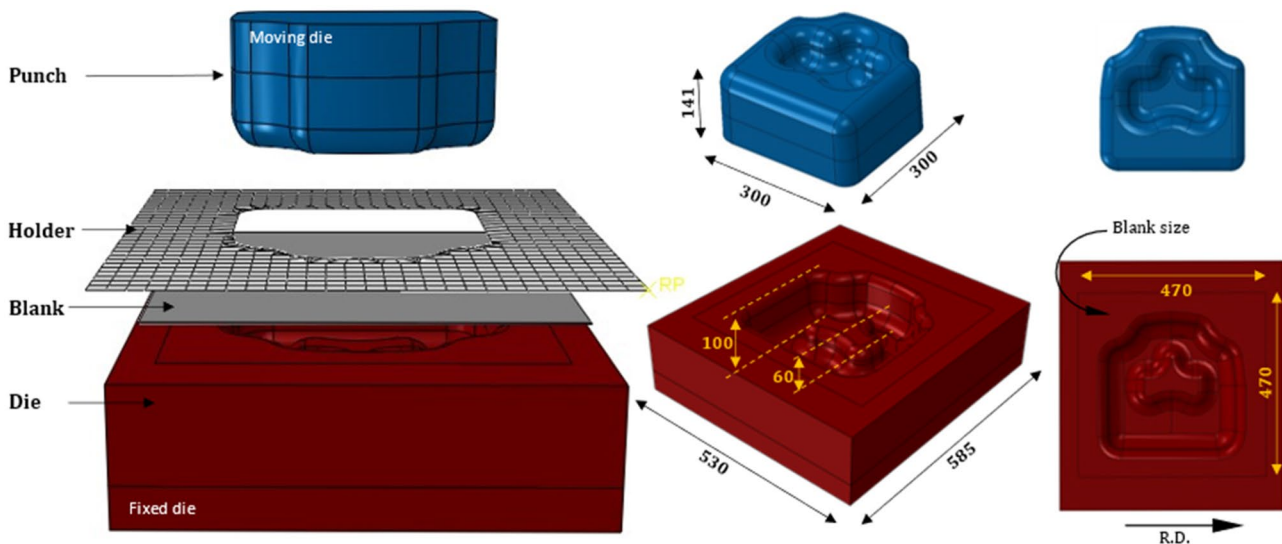


Fig. 9 Stamping dies assembly with die geometry and dimensions (mm)

1. Isotropic elasticity model with von Mises yield function and isotropic hardening model based on *XY* direction (0–90 fiber orientation) properties (Iso-XY).
2. Isotropic elasticity model with von Mises yield function and isotropic hardening model based on the *X* direction (± 45 fiber orientation) properties (Iso-X).
3. Orthotropic elasticity model with Hill 1948 anisotropic yield function and isotropic hardening model (Ortho).

In all three cases, linear elasticity model, von Mises yield function, and isotropic hardening model were assumed for DP 590 blank sheet. Hardening properties were obtained from uniaxial tension tests described in the previous section.

Progressive plastic deformation of the FDM polymer tool insert due to repeated stamping was estimated through FE simulations by a geometry update scheme. After each stamping simulation using ABAQUS/Explicit, an unloading simulation using ABAQUS/Standard was performed on the insert to obtain the plastic deformation.

The deformed insert shape along with the material state was used as the starting point for the next stamping simulation. This process was repeated until the plastic deformation reached saturation, and the additional plastic deformation was less than 5% from the previous stamping simulation.

5 Results and discussions

In both experiments and FE simulations, highest deformation is observed at the nose of the insert as shown in Fig. 14, which compares experimental deformation from ATOS scans after 100 hits and simulation deformation after a single stamping pass with material model “Iso-XY.” Magnitude of deformation is highly dependent on the tool material model used.

Figure 15 shows a comparison of the cumulative plastic deformation at the nose of the insert measured experimentally using ATOS scan to that obtained from FE simulations.

Fig. 10 a Conventional steel tools. b Steel die with polymer insert

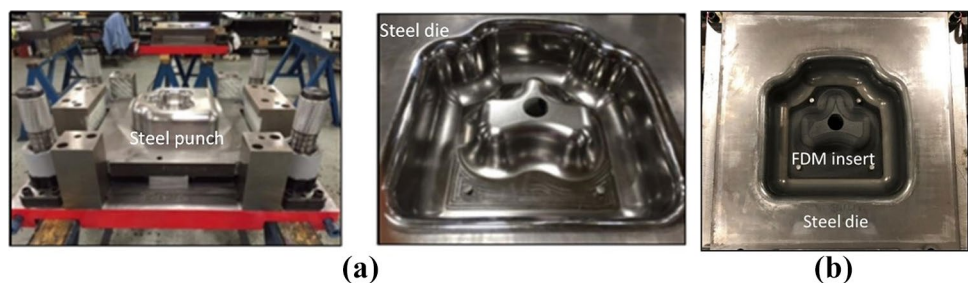
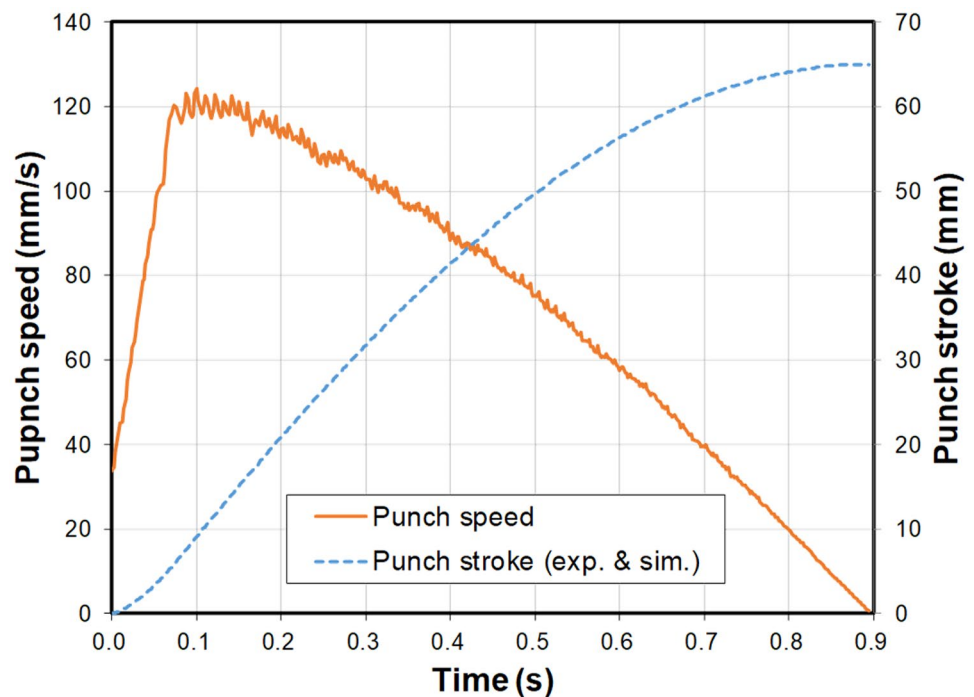


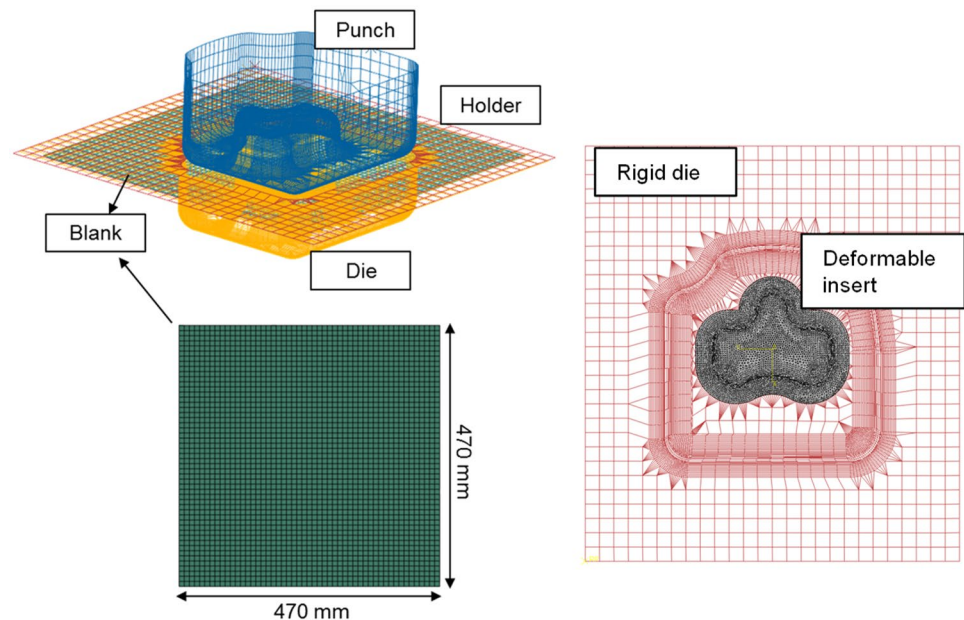
Fig. 11 Punch speed and punch stroke vs. time



Experimental data is only measured once after 100 stamping passes. However, FE simulation results with three different material models are shown for 3 stamping passes. Isotropic material model shows different results for different directions (Iso-X vs. Iso-XY), whereas orthotropic elastic material model with Hill 1948 yield function (Ortho) shows consistent results by accounting for the anisotropy in both elastic and plastic behavior.

Simulation results with orthotropic material model show higher deformation than experiments, suggesting that the material must be stronger than the model used for simulations. Figure 16 shows the calculated strain rate experienced by the FDM insert during a stamping pass, obtained from simulation results. Four points along the forming radius of the insert are selected for inspection. The observed strain rate at point #2 which shows the highest deformation is in the range of 10^{-1} to $10^{-2}/s$.

Fig. 12 FE simulation setup for steel and polymer tools



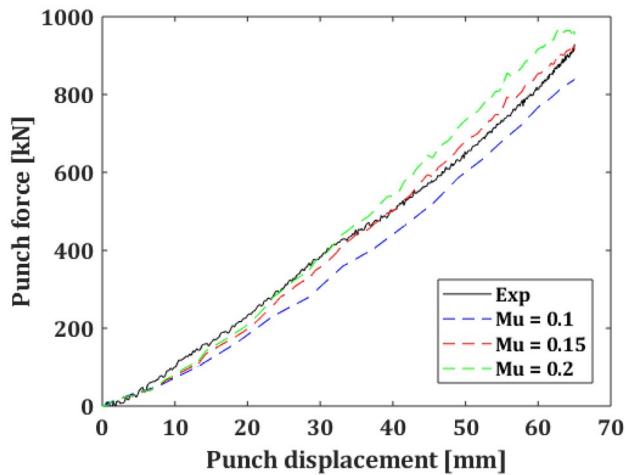


Fig. 13 Punch force vs. displacement for friction coefficient calibration

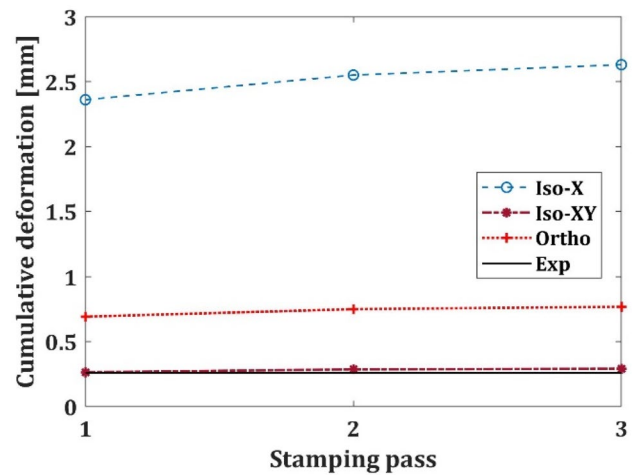


Fig. 15 Maximum cumulative deformation at the die insert nose from simulations and experiments

5.1 Strain rate dependency

The uniaxial tension and compression tests from the previous section used for simulations were performed at quasi-static strain rates of 10^{-4} /s. It is well known that polymers can exhibit strain rate sensitive behavior even at strain rates below 1/s and researchers have used strain rate-dependent material models that can capture this behavior [41]. As a preliminary investigation of the rate-sensitive behavior of CF-Nylon, additional uniaxial tension and compression tests were performed at a strain rate of 5×10^{-2} /s. Figures 17 and 18 show the true stress–strain plots for strain rates of $1e-4$ /s and $5e-2$ /s for uniaxial tension and compression, respectively. The preliminary testing results show clear strain rate dependency in CF-Nylon where both the elastic modulus and yield strength are increased with an increase in strain rate.

Table 7 summarizes the elastic properties for all four directions from uniaxial compression test at the strain rate of 5×10^{-2} /s. Using compression test results, Hill

1948 yield function coefficients are calculated as shown in Table 8.

Orthotropic elastic stiffness matrix was also recalibrated using experimental data obtained at the strain rate of $5e-2$ /s. FE simulation of stamping with polymer die insert was repeated with the new calibrated material properties from the high strain rate testing. Figure 19 shows the cumulative plastic deformation from simulation compared with experiment. The new material model predicts the die deformation with good accuracy. Although many areas within the AM tools may only experience low strain rates, the effect of using high strain rate properties is negligible as those areas experience very small strains. It is observed that the highest amount of tool deformation occurs in the very first stamping pass and the cumulative deformation reaches a steady state value within the first 3 passes. This observation is consistent with other researchers in the literature [8, 29]. Final stamped shape of the blank formed with polymer tools matches closely with that formed with steel tools as seen from the cross-sectional comparison shown in Fig. 20.

Fig. 14 Deformation on FDM insert after stamping from experiments and simulation (in mm)

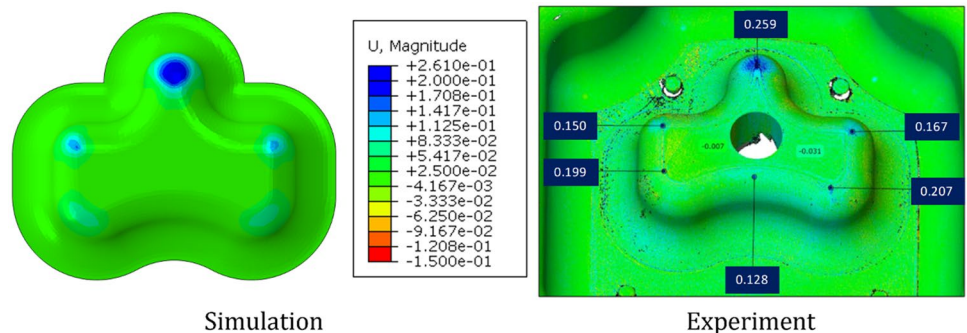


Fig. 16 Strain rate at critical points on FDM insert from FE simulations

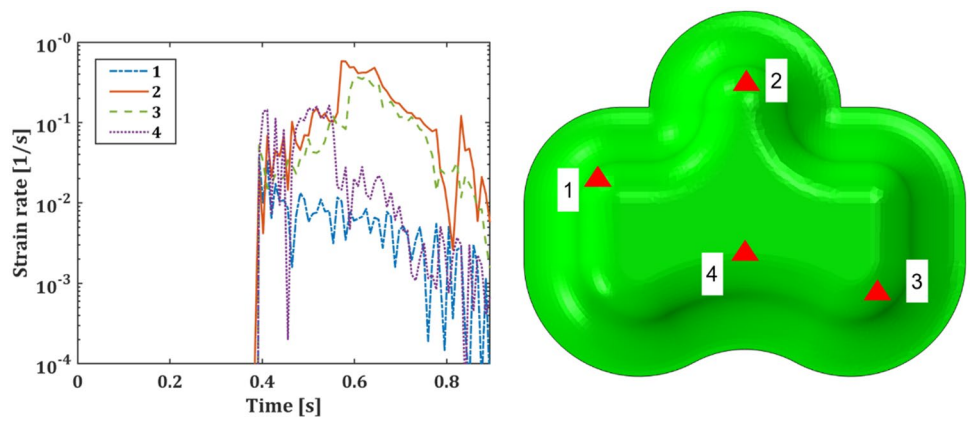


Fig. 17 Comparison of stress–strain behavior of CF-Nylon under uniaxial tension at strain rates of “S.R. 1 = $1e-4/s$ ” and “S.R. 2 = $5e-2/s$ ” for all tested directions

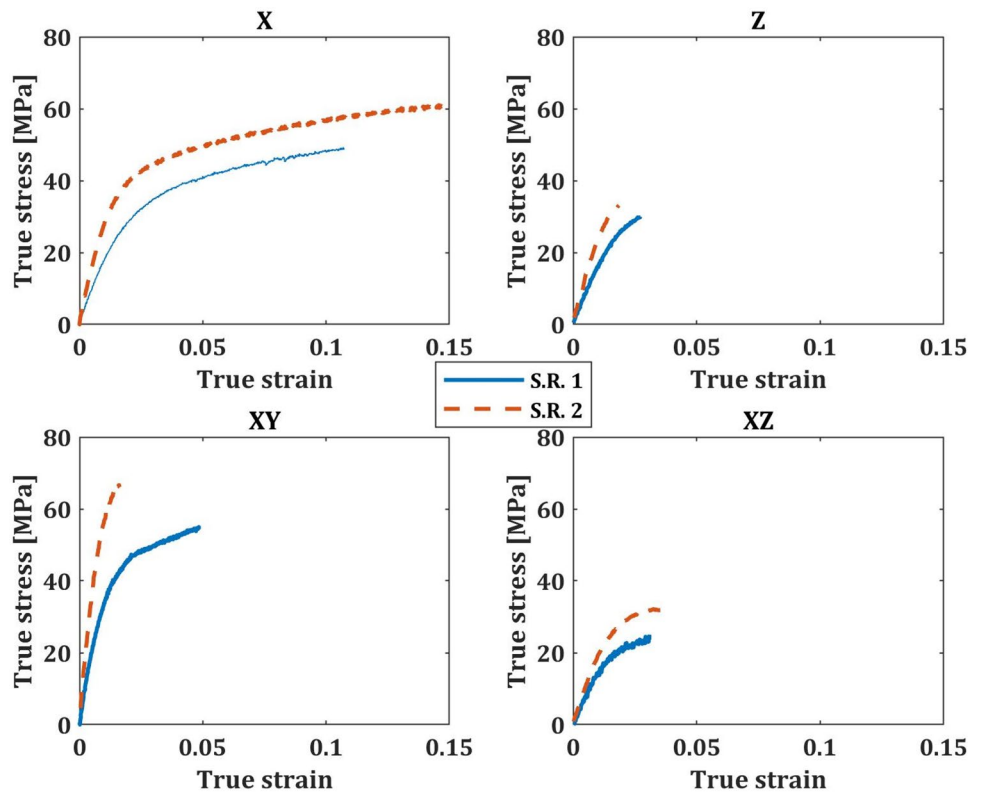


Fig. 18 Comparison of stress–strain behavior of CF-Nylon under uniaxial compression at strain rates of “S.R. 1 = 1e−4/s” and “S.R. 2 = 5e−2/s” for all tested directions

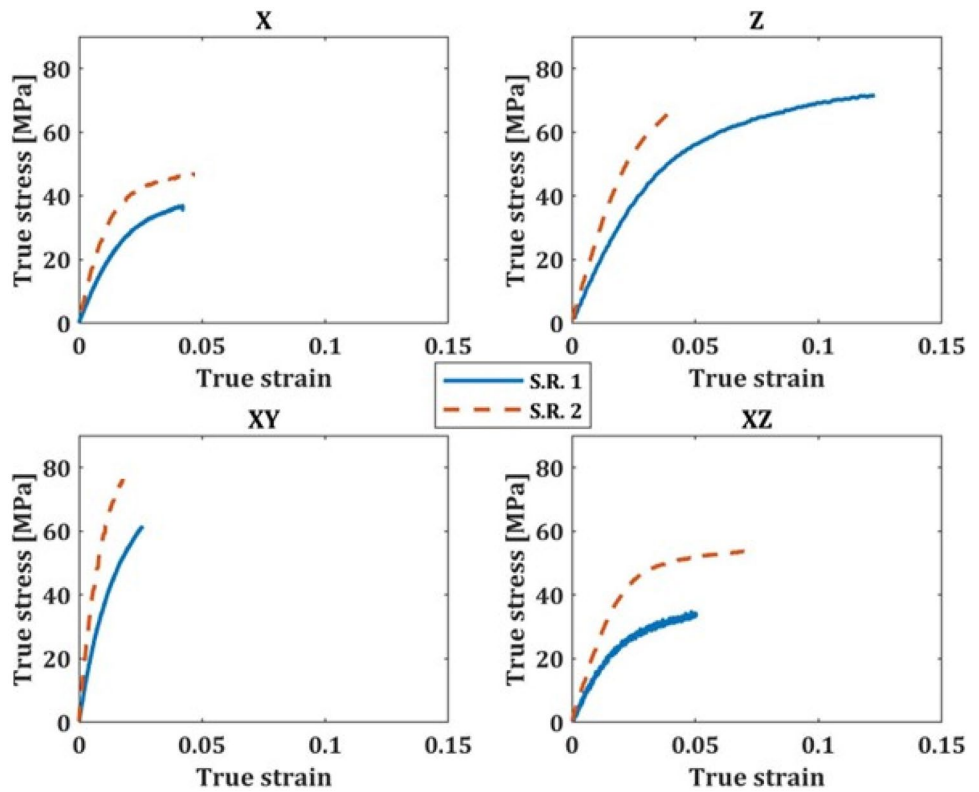


Table 7 Uniaxial compression results for strain rate $5 \times 10^{-2}/s$

| Property | Orientation | | | |
|-----------------------------------|----------------------------|----------------------------|--------------------------------|--------------------------------|
| | X | Z | XY | XZ |
| Young’s modulus (E) (GPa) | 3.12 ± 0.56 | 2.64 ± 0.11 | 7.35 ± 0.33 | 2.46 ± 0.08 |
| Poisson’s ratio (ν) | $\nu_{xy} = 0.61 \pm 0.08$ | $\nu_{zx} = 0.11 \pm 0.02$ | $\nu_{planar} = 0.10 \pm 0.01$ | $\nu_{planar} = 0.30 \pm 0.05$ |
| | $\nu_{xz} = 0.29 \pm 0.03$ | $\nu_{zy} = 0.13 \pm 0.04$ | | |
| Yield stress (σ_y) (MPa) | 32.9 ± 1.3 | 45.8 ± 2.2 | 58.2 ± 1.5 | 32.5 ± 1.6 |

Table 8 Calibrated coefficients for Hill 1948 yield criterion for strain rate of $5e−2/s$

| F | G | H | L | M | N |
|-----|-----|-------|-------|-------|-------|
| 0.5 | 0.5 | 1.633 | 2.452 | 2.452 | 0.820 |

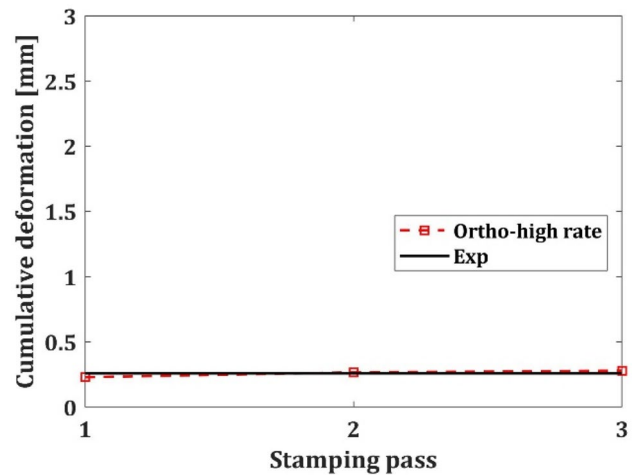
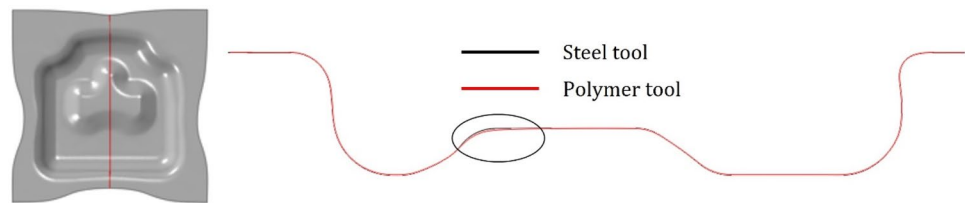


Fig. 19 Comparison of cumulative deformation at die insert nose from experiments and simulations using material properties at high strain rate

Fig. 20 Comparison of stamped blank shape from simulations using steel tools and FDM tools at the end of stamping stroke



6 Conclusions

CF-filled Nylon is a suitable tooling material for stamping of high-strength steels for low-volume production of up to 100 parts. There is only small amount of geometry change observed in the tool which could be the result of plastic deformation and wear. The tool geometry change did not affect the tool performance for low-volume stamping trial, and the final blank shape had only minor differences when compared to blanks formed with steel tooling. For FDM materials with chopped fiber reinforcements and orthogonal internal raster, tetragonal symmetry stiffness matrix accurately predicts the elastic behavior. Plastic behavior of FDM CF-Nylon is different in tension and compression due to the presence of voids inside the material. FDM CF-Nylon is strain rate sensitive for rates under 0.1/s and shows an increase in strength and stiffness as strain rate is increased. The use of orthotropic elastic material model with anisotropic yield is necessary for accurate prediction of tool performance. Further investigation of tool wear is necessary to investigate its contribution in tool dimension changes.

Appendix

Calibration of tetragonal symmetry compliance matrix

Reducing the Hooke's law for general anisotropic material using these symmetry operations, we get the following compliance matrix for tetragonal symmetry.

$$S = \begin{bmatrix} S_{11} & S_{12} & S_{13} & 0 & 0 & 0 \\ S_{12} & S_{11} & S_{13} & 0 & 0 & 0 \\ S_{13} & S_{13} & S_{33} & 0 & 0 & 0 \\ 0 & 0 & 0 & S_{44} & 0 & 0 \\ 0 & 0 & 0 & 0 & S_{44} & 0 \\ 0 & 0 & 0 & 0 & 0 & S_{66} \end{bmatrix} \quad (10)$$

We get 6 independent coefficients, which is a special case of orthotropic symmetry which has only 3 planes of

symmetry and 9 independent coefficients. These coefficients are calibrated using experimental data from tensile tests as follows. From uniaxial tension along X direction, we get Young's modulus E_x and following two Poisson's ratios.

$$\sigma_{xx} = E_x \epsilon_{xx}, \nu_{xy} = \frac{-\epsilon_{yy}}{\epsilon_{xx}}, \nu_{xz} = \frac{-\epsilon_{zz}}{-\epsilon_{xx}} \quad (11)$$

Using the condition of uniaxial tension along X direction in Hooke's law,

$$\begin{bmatrix} \epsilon_{xx} \\ \epsilon_{yy} \\ \epsilon_{zz} \\ \gamma_{yz} \\ \gamma_{zx} \\ \gamma_{xy} \end{bmatrix} = \begin{bmatrix} \epsilon_{xx} \\ -\nu_{xy}\epsilon_{xx} \\ -\nu_{xz}\epsilon_{xx} \\ \gamma_{yz} \\ \gamma_{zx} \\ \gamma_{xy} \end{bmatrix} = \begin{bmatrix} S_{11} & S_{12} & S_{13} & 0 & 0 & 0 \\ S_{12} & S_{11} & S_{13} & 0 & 0 & 0 \\ S_{13} & S_{13} & S_{33} & 0 & 0 & 0 \\ 0 & 0 & 0 & S_{44} & 0 & 0 \\ 0 & 0 & 0 & 0 & S_{44} & 0 \\ 0 & 0 & 0 & 0 & 0 & S_{66} \end{bmatrix} \begin{bmatrix} \sigma_{xx} \\ 0 \\ 0 \\ 0 \\ 0 \\ 0 \end{bmatrix}$$

Therefore,

$$S_{11} = \frac{E_{xx}}{\sigma_{xx}} = \frac{1}{E_x}; S_{12} = \frac{-\nu_{xy}}{E_x}; S_{13} = \frac{-\nu_{xz}}{E_x} \quad (12)$$

Performing similar operations for uniaxial tension along Y and Z directions, we get the following additional relations. Multiple experimental data from uniaxial tension along X , Y , and Z directions can be used to calculate the terms

$$S_{33} = \frac{1}{E_z}; S_{12} = \frac{-\nu_{xy}}{E_x} = \frac{-\nu_{yx}}{E_y}; \quad (13)$$

$$S_{13} = \frac{-\nu_{xz}}{E_x} = \frac{-\nu_{yz}}{E_y} = \frac{-\nu_{zx}}{E_z}$$

Using uniaxial tension condition along diagonal direction in XY plane in Hooke's law,

$$\begin{bmatrix} \frac{1}{2}\epsilon_{xy45_longitudinal} + \epsilon_{xy45_transverse} \\ \frac{1}{2}\epsilon_{xy45_longitudinal} + \epsilon_{xy45_transverse} \\ \epsilon_{zz} \\ 0 \\ 0 \\ \epsilon_{xy45_longitudinal} - \epsilon_{xy45_transverse} \end{bmatrix} = \begin{bmatrix} \frac{1}{2} \frac{1}{E_x} & -\frac{\nu_{xy}}{E_x} & -\frac{\nu_{xz}}{E_x} & 0 & 0 & 0 \\ -\frac{\nu_{xy}}{E_x} & \frac{1}{E_x} & -\frac{\nu_{xz}}{E_x} & 0 & 0 & 0 \\ \frac{1}{E_x} & -\frac{\nu_{xy}}{E_x} & -\frac{\nu_{xz}}{E_x} & 0 & 0 & 0 \\ \frac{1}{E_x} & -\frac{\nu_{xy}}{E_x} & -\frac{\nu_{xz}}{E_x} & 0 & 0 & 0 \\ 0 & 0 & 0 & S_{44} & 0 & 0 \\ 0 & 0 & 0 & 0 & S_{44} & 0 \\ 0 & 0 & 0 & 0 & 0 & S_{66} \end{bmatrix} = \begin{bmatrix} \frac{1}{2}\sigma_{xy45} \\ \frac{1}{2}\sigma_{xy45} \\ 0 \\ 0 \\ 0 \\ \frac{1}{2}\sigma_{xy45} \end{bmatrix}$$

where

$$\begin{aligned} \frac{1}{2}\epsilon_{xy45_longitudinal} &: \text{ tensile strain} \\ \frac{1}{2}\epsilon_{xy45_transverse} &: \text{ lateral strain} \\ \epsilon_{xy45} &: \text{ tensile stress} \end{aligned}$$

Here, the following two conditions must be satisfied for compatibility.

$$\begin{aligned} \epsilon_{xy45_longitudinal} + \epsilon_{xy45_transverse} &= \frac{(1 - \nu_{xy})}{E_x} \sigma_{xy45} \\ \epsilon_{zz} &= \frac{-\nu_{zx}}{E_z} \sigma_{xy45} \end{aligned}$$

We then get

$$S_{66} = \frac{2(\epsilon_{xy45_longitudinal} - \epsilon_{xy45_transverse})}{\sigma_{xy45}} \tag{14}$$

Similarly, for uniaxial tension along the diagonal direction in plane XZ (or YZ), we get

$$\begin{bmatrix} \frac{1}{2}\epsilon_{xz45_longitudinal} + \epsilon_{xz45_transverse} \\ \epsilon_y \\ \frac{1}{2}\epsilon_{xz45_longitudinal} + \epsilon_{xz45_transverse} \\ 0 \\ \epsilon_{xz45_longitudinal} + \epsilon_{xz45_transverse} \\ 0 \end{bmatrix} = \begin{bmatrix} \frac{1}{2} \frac{1}{E_x} & -\frac{\nu_{xy}}{E_x} & -\frac{\nu_{xz}}{E_x} & 0 & 0 & 0 \\ -\frac{\nu_{xy}}{E_x} & \frac{1}{E_x} & -\frac{\nu_{xz}}{E_x} & 0 & 0 & 0 \\ \frac{1}{E_x} & -\frac{\nu_{xy}}{E_x} & -\frac{\nu_{xz}}{E_x} & 0 & 0 & 0 \\ \frac{1}{E_x} & -\frac{\nu_{xy}}{E_x} & -\frac{\nu_{xz}}{E_x} & 0 & 0 & 0 \\ 0 & 0 & 0 & S_{44} & 0 & 0 \\ 0 & 0 & 0 & 0 & S_{44} & 0 \\ 0 & 0 & 0 & 0 & 0 & S_{66} \end{bmatrix} = \begin{bmatrix} \frac{1}{2}\sigma_{xz45} \\ \frac{1}{2}\sigma_{xz45} \\ 0 \\ 0 \\ 0 \\ \frac{1}{2}\sigma_{xz45} \end{bmatrix}$$

where

$$\begin{aligned} \epsilon_{xz45_longitudinal} &: \text{ tensile strain} \\ \epsilon_{xz45_transverse} &: \text{ lateral strain} \\ \sigma_{xz45} &: \text{ tensile stress} \end{aligned}$$

Here, the compatibility conditions and definition of S_{44} are as follows.

$$\begin{aligned} \epsilon_{xz45_longitudinal} + \epsilon_{xz45_transverse} &= \frac{(1 - \nu_{xz})}{E_x} \sigma_{xz45} \\ \epsilon_{yy} &= \frac{-\nu_{xy} - \nu_{xz}}{2E_x} \sigma_{xz45} \\ S_{44} &= \frac{2(\epsilon_{xy45_longitudinal} - \epsilon_{xy45_transverse})}{\sigma_{xy45}} \end{aligned} \tag{15}$$

In other words, shear modulus $G_{i,j}$ which is the inverse of the compliance matrix component S_{44} can be calculated by performing uniaxial tension test in the i - j plane along 45° and is defined as $G_{i,j} = \frac{E_k}{2(1+\nu_{kl})}$ where k is the tensile direction and l is the direction perpendicular to it in the ij plane.

Acknowledgements The authors wish to thank Honda R&D Americas, Inc. for their support of this project through university research funding (AWD-107099) under the strategic partnership agreement.

Funding This work was supported by university research funding (AWD-107099) from Honda R&D Americas Inc.

Declarations

Conflict of interest The authors declare no competing interests

References

1. Pourboghrat F, Zampaloni MA, Benard A (2003) Hydroforming of composite materials. US6631630B1. Available: <https://patents.google.com/patent/US6631630B1/en>. Accessed 12 Jan 2022
2. Thompson MK et al (2016) Design for additive manufacturing: trends, opportunities, considerations, and constraints. CIRP Ann 65(2):737–760. <https://doi.org/10.1016/j.cirp.2016.05.004>
3. Nakamura N, Mori K, Abe Y (2020) Applicability of plastic tools additively manufactured by fused deposition modelling for sheet metal forming. Int J Adv Manuf Technol 108(4):975–985. <https://doi.org/10.1007/s00170-019-04590-5>
4. Penumakala PK, Santo J, Thomas A (2020) A critical review on the fused deposition modeling of thermoplastic polymer composites. Compos B Eng 201:108336. <https://doi.org/10.1016/j.compositesb.2020.108336>
5. Dizon JRC, Espera AH, Chen Q, Advincula RC (2018) Mechanical characterization of 3D-printed polymers. Addit Manuf 20:44–67. <https://doi.org/10.1016/j.addma.2017.12.002>
6. Ahn H, Gingerich MB, Hahnen R, Dapino MJ, Pourboghrat F (2021) Numerical modeling of mechanical properties of UAM reinforced aluminum hat sections for automotive applications. Int J Mater Form 14. <https://doi.org/10.1007/s12289-020-01607-3>

7. Liewald M, de Souza JHC (2008) New developments on the use of polymeric materials in sheet metal forming. *Prod Eng Res Devel* 2(1):63–72. <https://doi.org/10.1007/s11740-008-0077-5>
8. Schuh G, Bergweiler G, Bickendorf P, Fiedler F, Colag C (2020) Sheet metal forming using additively manufactured polymer tools. *Procedia CIRP* 93:20–25. <https://doi.org/10.1016/j.procir.2020.04.013>
9. Hahnlen R, Pourboghraat F, Park T, Hoffman B, Athale M (2021) Additive manufacturing for sheet metal forming tools. *AHSS Guidelines*. <https://ahssinsights.org/forming/additive-manufacturing/additive-manufacturing-for-sheet-metal-forming-tools/>. Accessed 27 Oct 2021
10. Frohn-Sörensen P, Geueke M, Tuli TB, Kuhnhen C, Manns M, Engel B (2021) 3D printed prototyping tools for flexible sheet metal drawing. *Int J Adv Manuf Technol* 115(7):2623–2637. <https://doi.org/10.1007/s00170-021-07312-y>
11. Ersoy K, Çelik BB (2019) Utilization of additive manufacturing to produce tools. *IntechOpen*. <https://doi.org/10.5772/intechopen.89804>
12. Cao J et al (2019) Manufacturing of advanced smart tooling for metal forming. *CIRP Ann* 68(2):605–628. <https://doi.org/10.1016/j.cirp.2019.05.001>
13. Kuo C-C, Li M-R (2017) Development of sheet metal forming dies with excellent mechanical properties using additive manufacturing and rapid tooling technologies. *Int J Adv Manuf Technol* 90(1):21–25. <https://doi.org/10.1007/s00170-016-9371-0>
14. Al-Maharma AY, Patil SP, Markert B (2020) Effects of porosity on the mechanical properties of additively manufactured components: a critical review. *Mater Res Express* 7(12):122001. <https://doi.org/10.1088/2053-1591/abcc5d>
15. Mercado-Colmenero JM, Rubio-Paramio MA, la Rubia-Garcia MD, Lozano-Arjona D, Martin-Doñate C (2019) A numerical and experimental study of the compression uniaxial properties of PLA manufactured with FDM technology based on product specifications. *Int J Adv Manuf Technol* 103(5):1893–1909. <https://doi.org/10.1007/s00170-019-03626-0>
16. Crocchio D, De Agostinis M, Olmi G (2013) Experimental characterization and analytical modelling of the mechanical behaviour of fused deposition processed parts made of ABS-M30. *Comput Mater Sci* 79:506–518. <https://doi.org/10.1016/j.commatsci.2013.06.041>
17. Cantrell JT et al (2017) Experimental characterization of the mechanical properties of 3D-printed ABS and polycarbonate parts. *Rapid Prototyp J* 23(4):811–824. <https://doi.org/10.1108/RPJ-03-2016-0042>
18. Durgun I, Ertan R (2014) Experimental investigation of FDM process for improvement of mechanical properties and production cost. *Rapid Prototyp J* 20(3):228–235. <https://doi.org/10.1108/RPJ-10-2012-0091>
19. Somireddy M, Singh CV, Czekanski A (2020) Mechanical behaviour of 3D printed composite parts with short carbon fiber reinforcements. *Eng Fail Anal* 107:104232. <https://doi.org/10.1016/j.engfailanal.2019.104232>
20. Biswas P, Guessasma S, Li J (2020) Numerical prediction of orthotropic elastic properties of 3D-printed materials using micro-CT and representative volume element. *Acta Mech* 231(2):503–516. <https://doi.org/10.1007/s00707-019-02544-2>
21. Somireddy M, Singh CV, Czekanski A (2019) Analysis of the material behavior of 3D printed laminates via FFF. *Exp Mech* 59(6):871–881. <https://doi.org/10.1007/s11340-019-00511-5>
22. Li L, Sun Q, Bellehumeur C, Gu P (2002) Composite modeling and analysis for fabrication of FDM prototypes with locally controlled properties. *J Manuf Process* 4(2):129–141. [https://doi.org/10.1016/S1526-6125\(02\)70139-4](https://doi.org/10.1016/S1526-6125(02)70139-4)
23. Monaldo E, Marfia S (2021) Computational homogenization of 3D printed materials by a reduced order model. *Int J Mech Sci* 197:106332. <https://doi.org/10.1016/j.ijmecsci.2021.106332>
24. Kanouté P, Boso DP, Chaboche JL, Schrefler BA (2009) Multi-scale methods for composites: a review. *Arch Computat Methods Eng* 16(1):31–75. <https://doi.org/10.1007/s11831-008-9028-8>
25. Dialami N, Chiumenti M, Cervera M, Rossi R, Chasco U, Domingo M (2021) Numerical and experimental analysis of the structural performance of AM components built by fused filament fabrication. *Int J Mech Mater Des* 17(1):225–244. <https://doi.org/10.1007/s10999-020-09524-8>
26. Zhao Y, Chen Y, Zhou Y (2019) Novel mechanical models of tensile strength and elastic property of FDM AM PLA materials: experimental and theoretical analyses. *Mater Des* 181:108089. <https://doi.org/10.1016/j.matdes.2019.108089>
27. Schuh G, Bergweiler G, Fiedler F, Bickendorf P, Colag C (2019) A review on flexible forming of sheet metal parts. In 2019 IEEE International Conference on Industrial Engineering and Engineering Management (IEEM) pp 1221–1225. <https://doi.org/10.1109/IEEM44572.2019.8978879>
28. Zampaloni M, Pourboghraat F, Yu WR (2004). Stamp thermo-hydroforming: a new method for processing fiber-reinforced thermoplastic composite sheets. <https://doi.org/10.1177/0892705704038219>
29. Tondini F, Basso A, Arinbjarnar U, Nielsen CV (2021) The performance of 3D printed polymer tools in sheet metal forming. *Metals* 11(8). <https://doi.org/10.3390/met11081256>
30. Park Y, Colton JS (2003) Sheet metal forming using polymer composite rapid prototype tooling. *J Eng Mater Technol* 125(3):247–255. <https://doi.org/10.1115/1.1543971>
31. Klimyuk D, Serezhkin M, Plokhikh A (2021) Application of 3D printing in sheet metal forming. *Materials Today: Proceedings* 38:1579–1583. <https://doi.org/10.1016/j.matpr.2020.08.155>
32. Durgun I (2015) Sheet metal forming using FDM rapid prototype tool. *Rapid Prototyp J* 21(4):412–422. <https://doi.org/10.1108/RPJ-01-2014-0003>
33. Ahn H, Kuuttila NE, Pourboghraat F (2021) Effects of pressure, boundary conditions, and cutting reliefs on thermo-hydroforming of fiber-reinforced thermoplastic composite helmet based on numerical optimization. *J Thermoplast Compos Mater* 34(2):181–202. <https://doi.org/10.1177/0892705719842631>
34. Park Y, Colton JS (2005) Failure analysis of rapid prototyped tooling in sheet metal forming - cylindrical cup drawing. *J Manuf Sci Eng* 127(1):126–137. <https://doi.org/10.1115/1.1828054>
35. Data Sheet - EN FDM Nylon 12CF.pdf. Available: <https://info.stratasysdirect.com/rs/626-SBR-192/images/Data%20Sheet%20-%20EN%20FDM%20Nylon%2012CF.pdf>. Accessed 28 Oct 2021
36. Ahn H, Kuuttila N, Pourboghraat F (2018) Mechanical analysis of thermo-hydroforming of a fiber-reinforced thermoplastic composite helmet using preferred fiber orientation model. *J Compos Mater* 52:002199831876254. <https://doi.org/10.1177/0021998318762547>
37. Yu WR, Pourboghraat F, Chung K, Zampaloni M, Kang TJ (2002) Non-orthogonal constitutive equation for woven fabric reinforced thermoplastic composites. *Compos A Appl Sci Manuf* 33(8):1095–1105. [https://doi.org/10.1016/S1359-835X\(02\)00053-2](https://doi.org/10.1016/S1359-835X(02)00053-2)
38. Park T, Chung K (2012) Non-associated flow rule with symmetric stiffness modulus for isotropic-kinematic hardening and its application for earing in circular cup drawing. *Int J Solids Struct* 49(25):3582–3593. <https://doi.org/10.1016/j.ijssolstr.2012.02.015>
39. Chen Y, Zhao Y, Ai S, He C, Tao Y, Yang Y et al (2020) A constitutive model for elastoplastic-damage coupling effect of unidirectional fiber-reinforced polymer matrix composites. *Compos A Appl Sci Manuf* 130:105736
40. Cho J, Fenner J, Werner B, Daniel IM (2010) A constitutive model for fiber-reinforced polymer composites. *J Compos Mater* 44:3133–3150
41. Ahn H, Park T, Li Y, Yeo SY, Pourboghraat F (2021) Mechanical analysis of a thermo-hydroforming fiber-reinforced composite

using a preferred fiber orientation model and considering viscoelastic properties. J Manuf Sci Eng 144(2). <https://doi.org/10.1115/1.4051825>

Publisher's Note Springer Nature remains neutral with regard to jurisdictional claims in published maps and institutional affiliations.